

Geophysical Research Letters[®]



RESEARCH LETTER

10.1029/2024GL114414

Trans-Oceanic Distributed Sensing of Tides Over Telecommunication Cable Between Portugal and Brazil

Meichen Liu¹ , Luis Costa² , Pierre Mertz³, Siddharth Varughese³, Sumudu Edirisinghe³, Valey Kamalov⁴ , and Zhongwen Zhan¹ 

¹Seismological Laboratory, California Institute of Technology, Pasadena, CA, USA, ²NASA Jet Propulsion Laboratory, California Institute of Technology, Pasadena, CA, USA, ³Nokia, Savage, MD, USA, ⁴Valey Kamalov LLC, Gainesville, FL, USA

Key Points:

- We introduce a microwave-modulated distributed fiber sensing technique that turns a trans-Atlantic cable into an 81-sensor array
- The cost-effective microwave oscillator with superior low-frequency stability enables the detection of ocean tides
- We attribute the cable's tidal sensitivity primarily to Poisson's effect but also a significant temperature contribution locally

Supporting Information:

Supporting Information may be found in the online version of this article.

Correspondence to:

M. Liu,
meichenl@caltech.edu

Citation:

Liu, M., Costa, L., Mertz, P., Varughese, S., Edirisinghe, S., Kamalov, V., & Zhan, Z. (2025). Trans-oceanic distributed sensing of tides over telecommunication cable between Portugal and Brazil. *Geophysical Research Letters*, *52*, e2024GL114414. <https://doi.org/10.1029/2024GL114414>

Received 8 JAN 2025
Accepted 29 MAY 2025

Abstract Geophysical sensing in the open ocean is both costly and technically challenging. Here we developed a novel distributed fiber optic sensing technique that employs microwave modulation for phase measurement in signals returned from submarine repeaters. We transformed a trans-Atlantic telecom cable into an 81-sensor array and measured sub-millihertz strains. The strains correlate with ocean tide height variations in phase, suggesting a dominant factor of the cable's Poisson's effect. Large strains observed at fiber spans located in the shallow water match the strong variations of simulated seafloor temperature. This study presents the first experimental confirmation of detecting sub-millihertz signals using trans-oceanic distributed sensing with submarine cables at span-wise spatial resolution (~80 km), opening the potential for cost-efficient tsunami early warning and long-term ocean temperature monitoring compatible with active data-carrying fibers.

Plain Language Summary Monitoring pressure and temperature changes in the deep ocean is important for understanding climate, ocean circulation, and natural hazards. However, deploying and maintaining instruments on the seafloor is difficult and expensive. We developed a new method, trans-oceanic distributed sensing, that turns existing undersea telecommunication cables into geophysical sensors using fiber optic technology. This approach does not interfere with original communication functions and allows for long-term, wide-area monitoring. We tested it on a 5,900-km trans-Atlantic cable between Portugal and Brazil. The signals we recorded match predictions of ocean tide heights. We found that the cable stretches and contracts with pressure from ocean tides and responds to temperature changes in shallow regions. Our results show that this technique can detect very low-frequency ocean signals over long distances using infrastructure that already exists. With more than a million kilometers of submarine cables in place worldwide, this approach could provide a cost-effective way to monitor the ocean in real time, supporting applications such as tsunami early warning and long-term climate studies.

1. Introduction

Compared to terrestrial geophysical instrumentations, seafloor geophysical sensing remains challenging. Existing submarine sensing technologies in the open sea include costly ocean-bottom seismometers (e.g., Manuel et al., 2012) and Deep-ocean Assessment and Reporting of Tsunamis (DART) systems (Meinig et al., 2005), which are costly to deploy and even harder to maintain. DART also relies on uninterrupted satellite communication to provide tsunami early warning. Distributed Acoustic Sensing (DAS), which transforms fiber optic cables into dense arrays of vibration sensors via interferometry of Rayleigh backscattered light, has successfully expanded its application from terrestrial to submarine fiber sensing, detecting internal waves (Ide et al., 2021; Williams et al., 2023), earthquakes (e.g., Lindsey et al., 2019; Lior et al., 2021; Sladen et al., 2019; Williams et al., 2019), and high-frequency tsunamis (Tonogawa & Araki, 2024). However, DAS has two limitations for long-haul cables: (a) Rayleigh backscattering is filtered out by optical isolators in submarine repeaters, restricting submarine DAS to the first span (60–80 km) from the coast. (b) Although DAS has been shown to detect tidal and internal wave signals (Williams et al., 2023), the inherent 1/f noise in DAS limits sensitivity at sub-millihertz frequencies, complicating the monitoring of broadband, low-frequency oceanic phenomena.

An alternative way to overcome the range limitation of DAS is measuring the integrated changes over the entire cable length. Marra et al. (2018) and Zhan et al. (2021) detected seismic waves on transoceanic cables based on optical interferometry and polarization, respectively. However, both methods treat the entire submarine cable as a single sensor. Marra et al. (2022) innovatively proposed utilizing high-loss loop backs (HLLBs), which are

© 2025 The Author(s).

This is an open access article under the terms of the [Creative Commons Attribution-NonCommercial License](https://creativecommons.org/licenses/by-nc/4.0/), which permits use, distribution and reproduction in any medium, provided the original work is properly cited and is not used for commercial purposes.

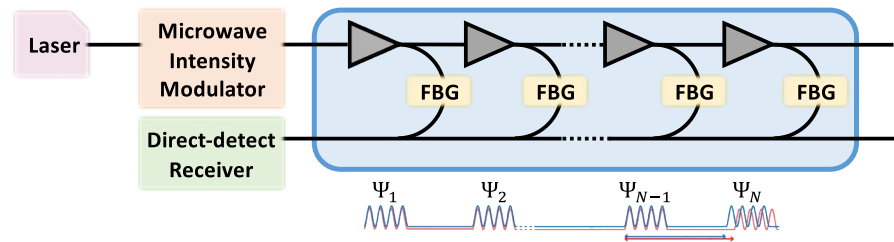


Figure 1. Measurement concept diagram. Optical signals are modulated by microwave intensity modulator, amplified by repeaters (gray triangles), reflected by Fiber Bragg Gratings (FBG), and detected by a direct-detect receiver. Red and blue waveforms depict the detected intensity of loop-back signals at different times, with Ψ representing corresponding phases at various repeaters.

essentially small reflectors within repeaters, to enable distributed sensing. They effectively transformed thousand-kilometer submarine cables into sensor channels spaced approximately 80 km apart. Employing HLLBs, Marra et al. (2022) and Costa et al. (2023) successfully located earthquakes using transoceanic cables, although challenges persist either from the hard requirements of ultra-stable laser sources for phase measurement, or from the non-linearity of polarization measurements with strain.

Limited by the inherent $1/f$ phase noise of optical laser sources, fiber optic sensing is typically most sensitive to frequencies at 1–10 Hz, sometimes down to a few millihertz. Microwave modulation, first introduced by Bogris et al. (2022) as Microwave Frequency Fiber Interferometry (MFFI), provides a cost-effective alternative that circumvents phase noise issues. This technique modulates the optical intensity to microwave frequency using non-stabilized lasers and requires minimal modifications to existing telecom infrastructure. More importantly, by utilizing microwave oscillators with superior long-term frequency stability compared to optical counterparts, microwave modulation can significantly enhance the detection of low-frequency signals, at the potential cost of reduced sensitivity at high frequencies.

To enable trans-oceanic distributed sensing (TODS) at low frequency, we developed a new instrument that also employs microwave modulation to achieve stable distributed sub-millihertz phase measurement along submarine cables containing HLLB repeaters. Instead of interferometry, we sample the optical intensity and measure the phase delay between consecutive reflections. We connected this instrument to a trans-Atlantic cable from Portugal to Brazil and captured signals at tidal frequencies along the 81-channel array.

2. Date and Methods

2.1. Instrument Architecture

Long-haul submarine telecommunication cables are equipped with repeaters about every 50–100 km to amplify the attenuated optical signals. Repeaters equipped with high-loss loop back (HLLB) paths couple a small amount of light to a Fiber Bragg Grating (FBG) (Figure 1) which routes light back toward the source through a second fiber. The return signals from HLLBs enable distributed fiber optic sensing along long-haul submarine cables, by measuring phase changes between consecutive reflections (Marra et al., 2022).

In MFFI (Bogris et al., 2022), the intensity (or envelope) of the launched pulses is modulated at some microwave frequency, and the phase change in the intensity is measured by interferometry with the local RF (radio frequency) modulation signal. Instead of interferometry, we use a direct-detect receiver that captures only the optical field intensity, not the phase, of the microwave-modulated wave. We then perform digital in-phase and quadrature (IQ) demodulation to measure the phase of intensity signals returned from HLLB paths, which are ultimately converted to strains of each cable span (For details, refer to Text S1 in Supporting Information S1).

In our configuration, the laser source is carved into 300 μs -long pulses (dictated by repeater separation), launched every 147 ms (dictated by submarine cable length), where each is modulated in intensity at radio frequency $f_{RF} = 90$ MHz. Shifting from traditional optic fiber sensing (196 THz) to microwave frequencies (90 MHz) reduced the period and sensitivity by about 2,000 times but significantly improves noise performance at sub-millihertz frequencies. Moreover, this microwave modulation technique is compatible with transponders used in data-carrying fibers, due to the relatively low-peak power and narrow bandwidth requirements.

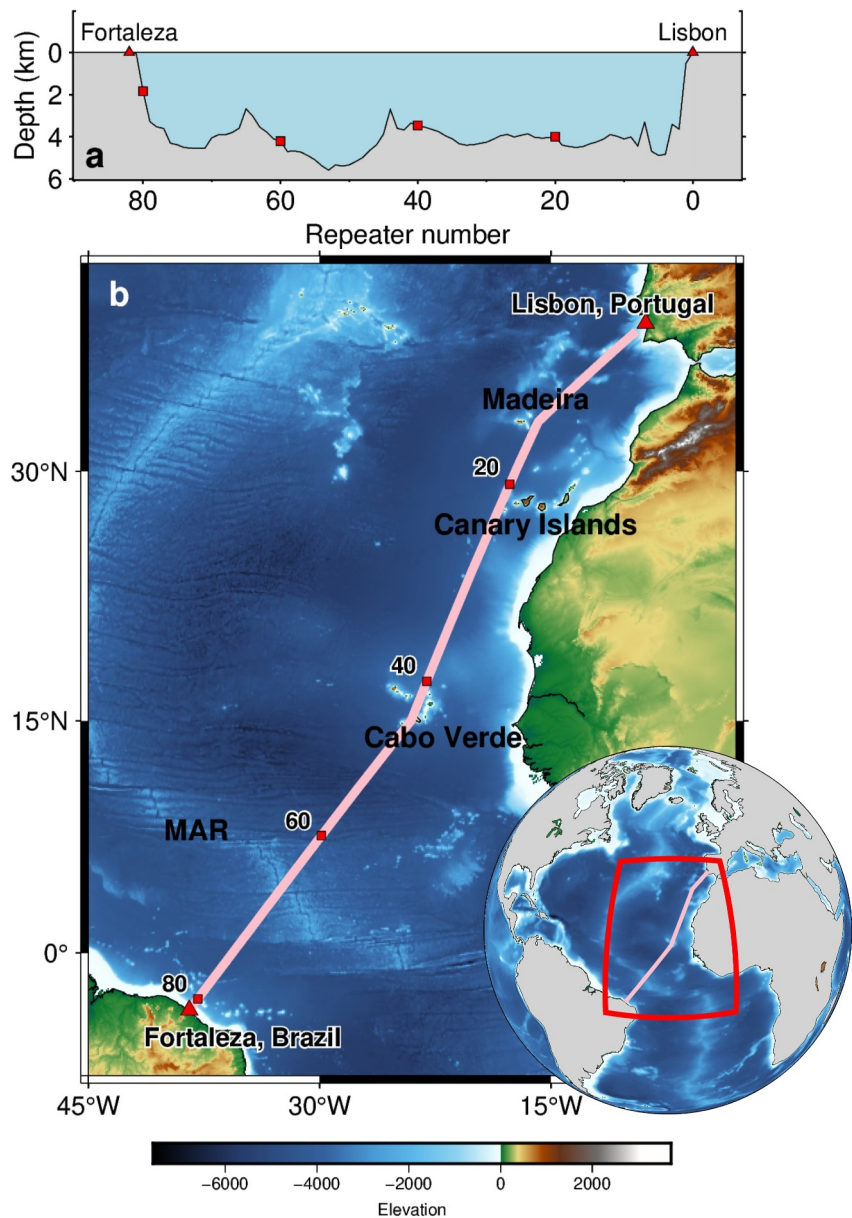


Figure 2. Map and bathymetry of Ellalink. (a) Cable bathymetry. (b) Cable trajectory, with the inset map providing a hemisphere view. Red triangles indicate two cable ends. Repeaters are denoted by squares and numbered every twentieth. Madeira, Canary Islands, Cabo Verde, and mid-Atlantic ridge, where the cable passes, are marked.

2.2. Data and Simulations

Our instrument was connected to the 5,900 km trans-Atlantic telecom cable, Ellalink, stretching from Portugal to Brazil (Figure 2b), equipped with 81 repeater-FBG units creating 82 spans. The cable traverses Madeira, Canary Islands, Cabo Verde, and mid-Atlantic ridge (MAR). Most of the cable is located below a depth of 3 km (Figure 2a), with the deepest section below 5 km, and the shallowest near Cabo Verde and MAR. We collected 77-day of data starting from 19 June 2024 and removed glitches and outliers (detailed in Text S1 in Supporting Information S1). We compared our observation to the averaged ocean tide heights predicted from GOT4.10c (Ray, 2013) and the seafloor temperature predicted in the GEOS-MITgem C1440-LLC2160 simulation (Strobach et al., 2022; Torres et al., 2022) (see details in Text S2 in Supporting Information S1).

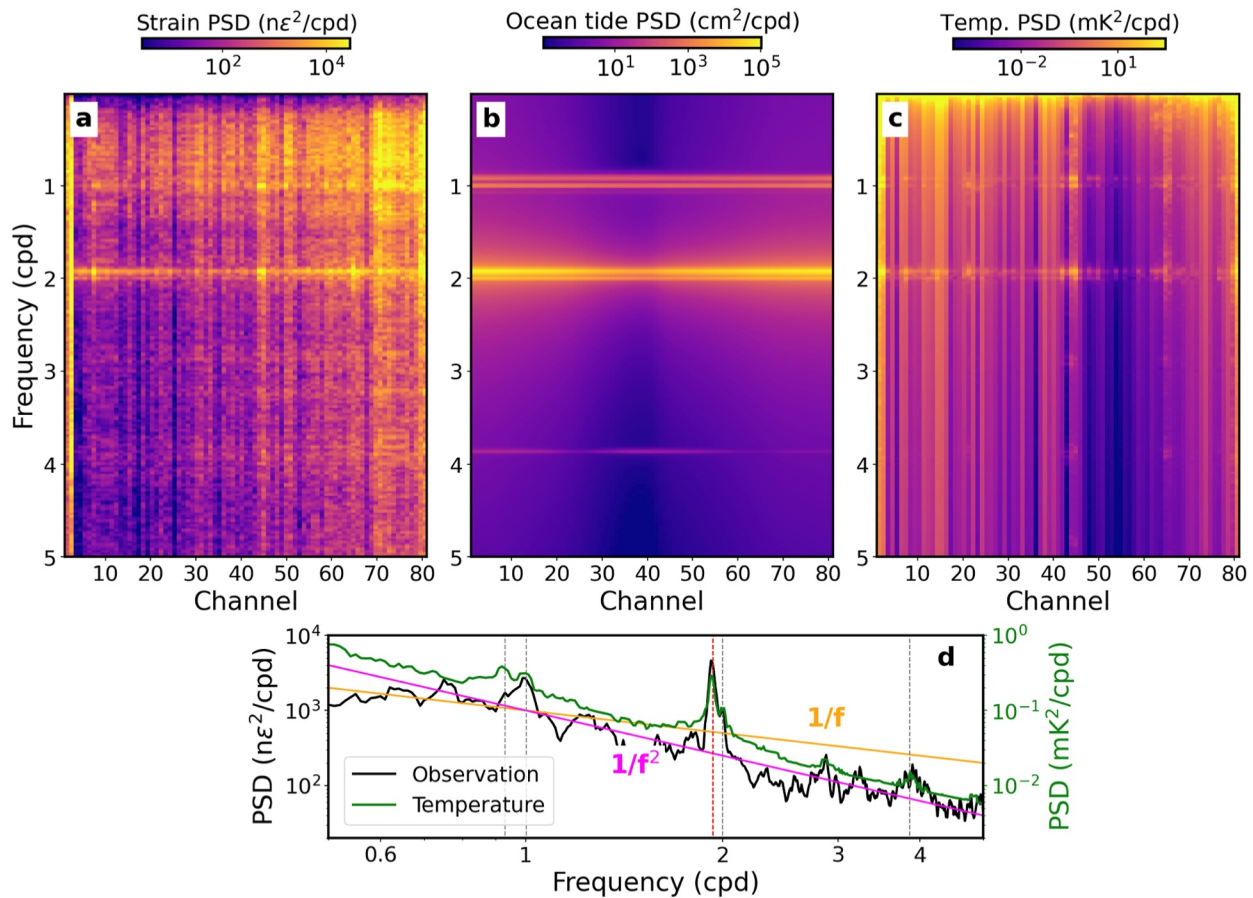


Figure 3. Top row: average power spectral densities (PSDs) of (a) observed strain, (b) synthetic ocean tide height, and (c) simulated seafloor temperature variation. Bottom: (d) median PSDs of observed strain (black) and seafloor temperature variation (green). Dashed vertical lines mark diurnal (O_1 , K_1), semidiurnal (M_2 , S_2), and quarter-diurnal (M_4) tidal modes, with the M_2 mode (1.93 cpd) highlighted in red. The orange and magenta lines indicate $1/f$ and $1/f^2$ decay slopes. Frequencies are in cycles per day (cpd).

3. Results

3.1. Spectral Analysis

We first explored the broadband spectral content of the observations and simulations. We computed for each channel the power spectral density (PSD) using a 38-day sliding window and took the average as the final PSD (Figures 3a–3c). The median PSD across all channels was then calculated at each frequency (Figure 3d) to extract the common trend with frequency for further comparison.

Among tidal periods, semidiurnal peaks, especially the M_2 mode, are most prominent in the observed strain (Figure 3a), synthetic tide heights (Figure 3b), and the simulated seafloor temperature (Figure 3c). Diurnal peaks are less prominent in the observed strain but are comparable in amplitude to semidiurnal peaks in the simulated temperature. The quarter-diurnal peaks are mostly indistinguishable.

At non-tidal periods, median PSDs (Figure 3d) show a similar $1/f^2$ decay above 0.8 cpd for both strain and temperature variation, steeper than typical $1/f$ slope of oceanic processes. Along the cable, temperature variation is lowest near channel 50–60 (Figure 3c), whereas strain is lowest at lower channel numbers (Figure 3a). Note that non-tidal contents of synthetic tides (Figure 3b) are artifacts of Fourier processing. The temperature variation pattern reflects the combined influence from water depth and bathymetry: deep-ocean stratification makes water temperature depth-dependent, while sharper bathymetric gradients enhance temperature variability through water movement. Channels with greater depth and smoother topography show smaller temperature variations (e.g., channels 50–60) and vice versa (e.g., channels 0–20). In contrast, the spatial pattern of observed strain remains

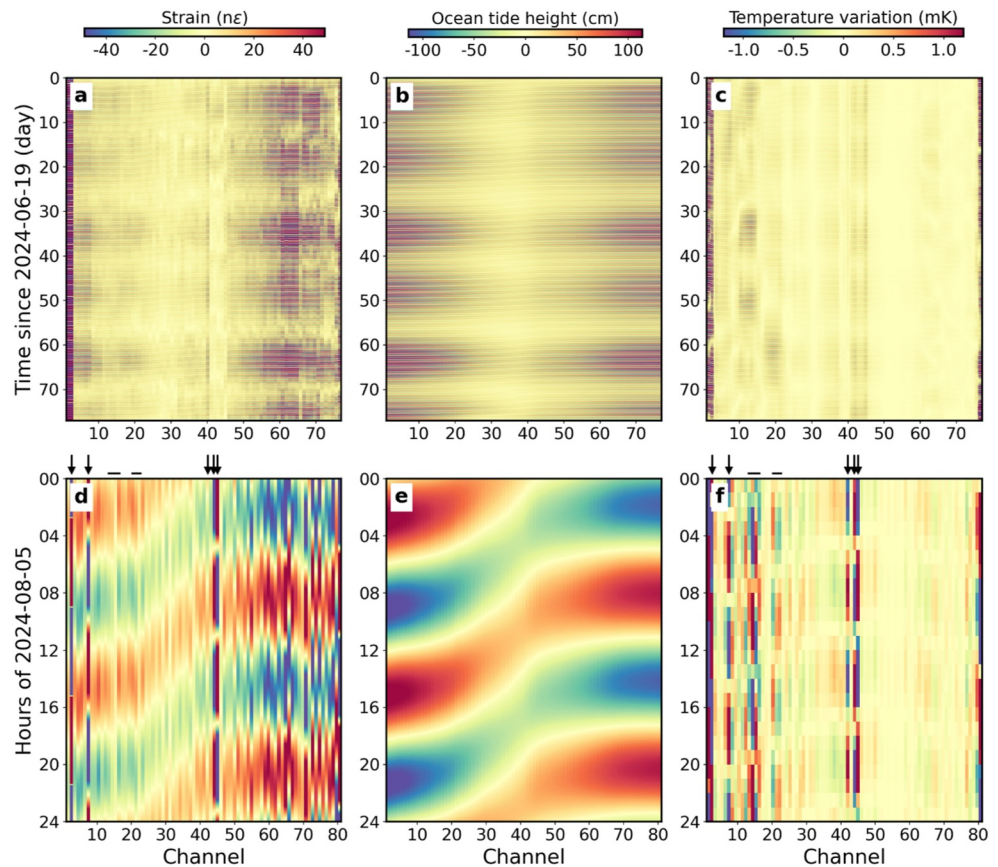


Figure 4. Top row: 77 days of (a) observed strain, (b) synthetic ocean tide height, and (c) simulated seafloor temperature variation, smoothed over five spans. Bottom row: same as top row but for 5 August 2024, smoothed over one span. All panels are filtered between 11 and 13 hr. Black arrows and bars in panels (d, f) indicate channels 2, 7, 13–16, 20–22, 42, 44, and 45 sequentially.

unexplained. Simulated sea surface height (Figure S6a in Supporting Information S1), though including various ocean processes, remains tide-dominated and does not explain the pattern. In the subsequent sections, non-tidal components are not our focus.

3.2. Temporal Analysis

Given the dominant energy at semidiurnal period across the cable, we applied a bandpass filter (11–13 hr) to the observed strain, synthetic ocean tide height, and simulated seafloor temperature for time-domain analysis. We also filtered to diurnal and quarter-diurnal period (Figures S7 and S8 in Supporting Information S1) but found there is little correlation among the three data sets.

Over the recording period, both the strain and ocean tide height show fortnightly amplitude modulation with aligned peaks and troughs (Figures 4a and 4b). On a daily scale, the strain is well aligned in phase with ocean tide height (Figures 4d and 4e), capturing the tide propagation between Portugal and Brazil. These correlations imply that our observation is strongly influenced by ocean tides at semidiurnal period. However, the strain amplitudes deviate from the spatial pattern of synthetic tide heights, which peak near the coast and reach a minimum around channel 40. This discrepancy is further discussed in Section 4.

In contrast, the simulated seafloor temperature variation exhibits weak phase alignment with the observed strain (Figure 4f) and limited fortnightly modulation (Figure 4c), along with greater amplitude variability between adjacent channels (Figures 4d and 4f). At some shallow locations, such as channel 2 across the continental shelf and channels 7, 44, and 45 crossing islands, larger simulated temperature variations correspond to larger observed strains. However, in other shallow or topographically complex regions, such as channels 60–70 crossing MAR,

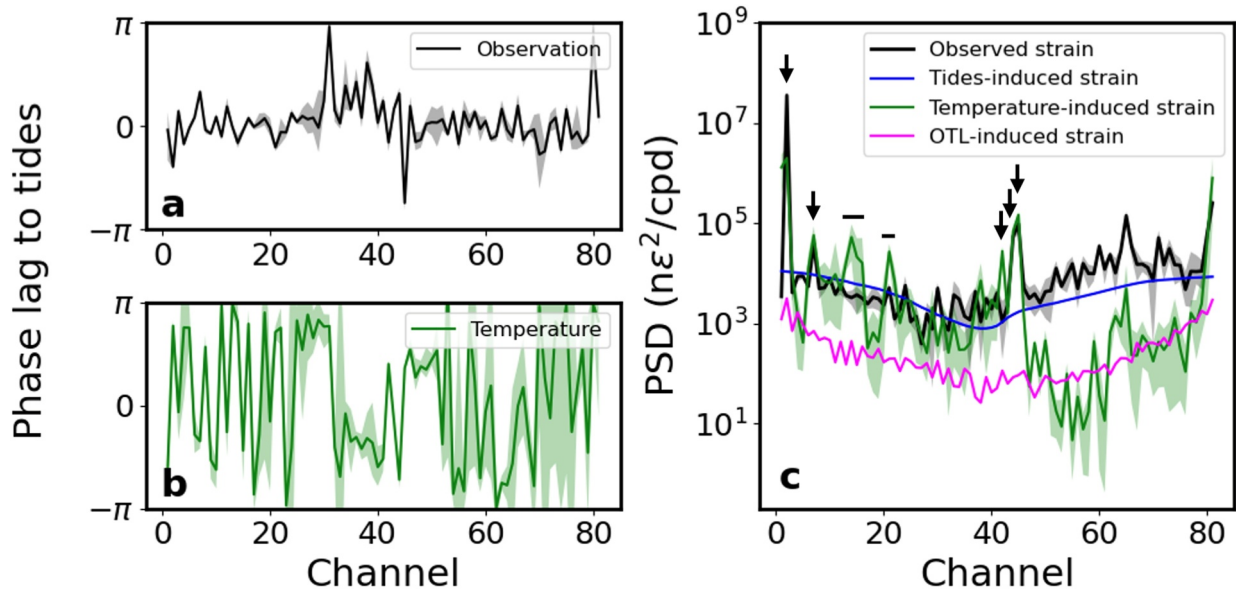


Figure 5. (a) Phase difference at M_2 mode between synthetic ocean tide heights and the observed strain. (b) Same as panel (a) but for simulated seafloor temperature. (c) Average power spectral density at M_2 mode for the observed strain (black), Poisson effect-induced (blue), temperature-induced (green), and ocean-tide-loading (ocean-tide loading)-induced (magenta) strain. Shadings represent the 5%–95% range across 38 moving windows. Arrows and bars in panel (c) mark the same channels as in Figure 4.

13–16 near Madeira, 20–22 near the Canary Islands, and 42 closes to Cabo Verde, large, simulated temperature variations do not coincide with strong strain signals.

In summary, at the semidiurnal period, the observed strain is phase-aligned with ocean tide heights, and the temperature variation matches at some shallow channels. In the following section, we focus on semidiurnal signals to further investigate the origin of the observed strain response.

4. Discussions

Trans-oceanic distributed sensing (TODS) remains in its early stage. The strain of the long-haul submarine fiber is influenced by multiple effects, including cable's Poisson effect (Kojima et al., 1982; Moeller, 2023; Tatekura et al., 1982), seafloor compliance (Becerril et al., 2024; Crawford et al., 1991), water temperature (Becerril et al., 2024; Ide et al., 2021; Williams et al., 2023), whereas the dominant influences remain unclear. Here, we evaluate the contributions of these factors based on our observations and analysis to improve the interpretation of submarine fiber sensing data.

4.1. Poisson's Effect

In Figure 5a, despite some discrepancies from noise, temperature, or coupling issues, the observed strain and synthetic tides are generally phase-aligned. Ocean tides could affect the cable via Poisson's effect, where barotropic pressure changes alter cable length. To evaluate this effect, we estimate the pressure-strain relationship by modeling the cable as thick-walled vessels under uniform hydraulic pressure with open ends (Moeller, 2023; Young et al., 2002):

$$\epsilon = \frac{2\nu}{E} \frac{r_0^2}{r_0^2 - r_i^2} \Delta P \quad (1)$$

where E is the Young's modulus, $\nu = 0.25$ is the Poisson's ratio, and $\Delta P = \rho g \Delta h$ is the pressure changes where $\rho = 1,025 \text{ kg/m}^3$ is water density, $g = 9.81 \text{ m/s}^2$ is gravitational acceleration, and Δh is ocean tide height. r_0 and r_i are the outer (fiber and cable armor) and inner (fiber) radii of the cable. We simplify the ratio of radii as $r_0^2/(r_0^2 - r_i^2) = 2$. Linear regression between observed strain and tidal height yields channel-specific estimates of

Young's modulus (Figure S9 in Supporting Information S1), which are generally higher for lower channel numbers. This aligns with the amplitude discrepancy in Figures 4d and 4e. The cause of this spatial variation remains unclear. We have examined potential factors such as cable armoring, seafloor topography, and plate age, but found no clear correlation.

We compute a 10% trimmed mean and standard deviation, resulting in 323 ± 110 GPa, corresponding to $\epsilon/\Delta p = 3.1 \times 10^{-12} \text{ Pa}^{-1}$. The resulting PSD of Poisson-effect-induced strain, as shown by the blue line in Figure 5c, broadly follows the trend of observed strain trend. This scaling obtained from TODS is two orders of magnitude smaller than DAS observations in Williams et al. (2023) and approximately one order of magnitude smaller than the normalized value reported by Tonegawa and Araki (2024), but is closer to that measured from trans-oceanic integrated sensing in Moeller (2023). Moeller (2023) found the cable stretched when high tides and obtained a Young's modulus of 200 GPa along a trans-Pacific cable.

The Young's modulus of long-haul submarine cables remains poorly constrained due to their complex, multi-layered construction, with 2–6 GPa for HDPE layer and about 200 GPa for steel wires. Becerril et al. (2024) used values of 5–50 GPa based on shallow water cable (<1,500 m) without repeaters (Kojima et al., 1982; Tatekura et al., 1982), which may not reflect real conditions in the open sea. In practice, long submarine cables experience bending, kinking, and mixed mechanical and thermal states, complicating the interlayer stress and strain transfer functions. Additionally, a change in Young's modulus from 25 to 300 GPa alters strain by an order of magnitude, an effect that may be masked by factors such as cable coupling. Thus, while cable's Poisson effect likely contributes significantly to our observations, we remain cautious in inferring Young's modulus of the long submarine cable from our data.

4.2. Ocean-Tide-Loading Induced Earth Response

Seafloor deformation from ocean-tide loading (OTL) can also induce strain in the cable. Due to the long wavelengths and low frequencies of ocean tides, compliance (Crawford et al., 1991) is not applicable (Zumberge et al., 2018) in our case. Instead, we consider the OTL response of a spherical Earth, as it has been observed on land (Martens et al., 2016), suggesting detectability in the ocean.

We used LoadDef (Martens et al., 2019) to model the OTL-induced strain of 1D SNREI earth model (detailed in Text S2 in Supporting Information S1) assuming full coupling with the seafloor. The resulting strain (Figure S3 in Supporting Information S1) closely resembles ocean tide height patterns, but is ~ 3 times smaller in amplitude than observed. Its M_2 -mode PSD is shown in Figure 5c. Varying the lithosphere thickness between 10 and 170 km altered the OTL-induced strain by less than 20%, suggesting limited sensitivity of 1D models. Given the lateral heterogeneity along the cable path, 3D modeling is needed for more accurate estimates.

The OTL-induced response has opposite polarity to the Poisson effect. To calibrate polarity, we referenced DAS observations from Williams et al. (2023) and trans-Pacific results by Moeller (2023), as no lab tests exist for long-haul telecom cables. After calibrations, our observations show high strains aligned with high tides, consistent with Poisson effect predictions. However, we would like to note that, Zumberge et al. (2018) reported contraction under high tides using a 200-m tensioned cable, whereas Araki et al. (2024) observed inconsistent polarity across three sites. Further investigation is needed to fully resolve the polarity in long-haul submarine fiber sensing.

4.3. Temperature Effect

Temperature influences the measured phase and thus strain by altering the fiber's refractive index. In shallow coastal regions, temperature variations tend to dominate the DAS signal (Ide et al., 2021; Pelaez Quiñones et al., 2023; Williams et al., 2023). In contrast, at greater depths (e.g., 3 km along our cable), temperature plays a less dominant role. The M_2 -phase mismatch between temperature variation and strain (Figure 5b), along with the weak correlation between temperature and pressure in DART records (Figures S4a and S4b in Supporting Information S1), despite spectral peaks at tidal frequencies (Figures S4c and S4d in Supporting Information S1), suggest that the strain-tide phase alignment is not driven by temperature.

A linear fit of simulated seafloor temperature variations to the observed strain yields a thermal strain scaling of $\Delta T/\epsilon \approx 5.8 \times 10^{-5} \text{ K}$, higher than the typical DAS sensitivity of $\Delta T/\epsilon \approx 1.1 \times 10^{-5} \text{ K}$ (Koyamada et al., 2009), suggesting there could be additional contributing factors beyond temperature variation. Using the scale, we compute the M_2 -mode thermal-induced strain PSD (Figure 5c). While the result matches the amplitude

or trend at some shallow channels (e.g., 2, 7, 44, and 45), much of the channel-to-channel variability remains unexplained. This mismatch may stem from limitations in the temperature simulation due to low vertical resolution (Text S1 in Supporting Information S1), or from unmodeled effects such as sediment layer or cable burial.

Figures 3d and S4d in Supporting Information S1 show that the spectral slope of the observed strain at non-tidal frequencies closely matches that of the temperature variation, suggesting possible influence from temperature fluctuations. However, similar spectral slopes could also arise from other sources. First, DART (Figure S4d in Supporting Information S1) and simulated sea surface height (Figure S6c in Supporting Information S1), both incorporating a wide range of ocean dynamics such as eddies, internal waves, and currents, follow a near $1/f$ spectra. Second, $1/f$ instrumental noise may also contribute. Thus, whether the observed non-tidal slope is driven by temperature or by a combination of all remains uncertain. This is worth further investigation, as it holds the potential for monitoring subtle seafloor temperature changes over extended timescales.

4.4. Challenges and Opportunities for Future Work

Our analysis indicates that the observed strain is primarily driven by the Poisson effect of the cable in response to ocean tides, with temperature variations dominating in shallow regions. Remaining amplitude discrepancies may reflect contributions from cable coupling and seafloor sediments, which require further investigation and is beyond the scope of this study.

Observation of pressure-induced strain with TODS in the deep ocean highlights its potential for tsunami early warning. TODS observations of infragravity waves with shorter wavelengths are likely aliased due to the long gauge length, but long-wavelength tsunamis are in principle detectable. Tsunamis with 10–20 min period and speed ~ 200 m/s have wavelengths of 120–240 km, spanning 2–5 repeaters. The comparison with the 2011 Tohoku tsunami (Figure S10 in Supporting Information S1) indicates that the TODS noise level would need to be reduced by two orders of magnitude across the tsunami frequency band (~ 3 min–3 hr) to detect a comparable signal. Our next-generation TODS system aims to achieve >100 -fold performance improvement through higher microwave oscillator frequency and coherent detection. Therefore, with noise reduced substantially, TODS has the potential to contribute to future tsunami detection.

5. Conclusions

We developed a microwave modulated optic fiber sensing technique for TODS. The technique converted the trans-Atlantic Ellalink cable between Portugal and Brazil into an 81-sensor array, to measure sub-millihertz signals. The observed strain highly correlates with semidiurnal ocean tides height variation, indicating cable stretching and shortening due to barotropic pressure change. Larger strains observed at some channels are likely attributed to greater temperature variations at shallow depth.

We demonstrate a cost-effective and non-disruptive method for low-frequency seafloor pressure and temperature monitoring. This first-generation instrument, incorporating a microwave intensity modulator and a direct-detect receiver, operates within a narrow, non-telecom spectrum thus noninvasive to telecom traffic. A second-generation system is under development to improve sensitivity and signal-to-noise ratio. Although this study focuses on tidal signals, this finding opens the possibility that, with the extensive network of underutilized submarine cables and future improvements in instrument, TODS could be used for tsunami early warning and long-term ocean temperature monitoring.

Data Availability Statement

Fiber optic data are available through CaltechDATA via M. Liu (2025).

References

- Araki, E., Kinoshita, M., Yokobiki, T., Nishida, S., Machida, Y., Matsumoto, H., et al. (2024). Fiber optic strain sensing networks in the seafloor and the deep seafloor borehole in Nankai Trough subduction zone. In *AGU24* (pp. S43D–3462).
- Becerril, C., Sladen, A., Ampuero, J. P., Vidal-Moreno, P. J., Gonzalez-Herreraez, M., Kutschera, F., et al. (2024). Towards tsunami early-warning with Distributed Acoustic Sensing: Expected seafloor strains induced by tsunamis. *Authorea Preprints*.
- Bogris, A., Nikas, T., Simos, C., Simos, I., Lentas, K., Melis, N. S., et al. (2022). Sensitive seismic sensors based on microwave frequency fiber interferometry in commercially deployed cables. *Scientific Reports*, *12*(1), 14000. <https://doi.org/10.1038/s41598-022-18130-x>
- Costa, L., Varughese, S., Mertz, P., Kamalov, V., & Zhan, Z. (2023). Localization of seismic waves with submarine fiber optics using polarization-only measurements. *Communications Engineering*, *2*(1), 86. <https://doi.org/10.1038/s44172-023-00138-4>

Acknowledgments

We are grateful to Ellalink for supporting long-term data collection, and Vincent Gatineau and Diego Matas for their interest and comments. We thank Joern Callies for guidance on seafloor temperature simulations and Simone Puel and Hilary Martens for advice on OTL Earth response. We thank the editor Daoyuan Sun and two anonymous reviewers for their constructive comments. This work was supported by NSF CAREER Award 1848166 and the Moore Foundation.

- Crawford, W. C., Webb, S. C., & Hildebrand, J. A. (1991). Seafloor compliance observed by long-period pressure and displacement measurements. *Journal of Geophysical Research: Solid Earth*, 96(B10), 16151–16160. <https://doi.org/10.1029/91jb01577>
- Ide, S., Araki, E., & Matsumoto, H. (2021). Very broadband strain-rate measurements along a submarine fiber-optic cable off Cape Muroto, Nankai subduction zone, Japan. *Earth Planets and Space*, 73(1), 1–10. <https://doi.org/10.1186/s40623-021-01385-5>
- Kojima, N., Yabuta, T., Negishi, Y., Iwabuchi, K., Kawata, O., Yamashita, K., et al. (1982). Submarine optical fiber cable: Development and laying results. *Applied Optics*, 21(5), 815–821. <https://doi.org/10.1364/ao.21.000815>
- Koyamada, Y., Imahama, M., Kubota, K., & Hogari, K. (2009). Fiber-optic distributed strain and temperature sensing with very high measurement resolution over long range using coherent OTDR. *Journal of Lightwave Technology*, 27(9), 1142–1146. <https://doi.org/10.1109/jlt.2008.928957>
- Lindsey, N. J., Dawe, T. C., & Ajo-Franklin, J. B. (2019). Illuminating seafloor faults and ocean dynamics with dark fiber distributed acoustic sensing. *Science*, 366(6469), 1103–1107. <https://doi.org/10.1126/science.aay5881>
- Lior, I., Sladen, A., Rivet, D., Ampuero, J. P., Hello, Y., Becerril, C., et al. (2021). On the detection capabilities of underwater distributed acoustic sensing. *Journal of Geophysical Research: Solid Earth*, 126(3), e2020JB020925. <https://doi.org/10.1029/2020jb020925>
- Liu, M. (2025). Dataset for TODS (1.0.0) [Dataset]. *CaltechDATA*. <https://doi.org/10.22002/4ms8e-8nc29>
- Mãnuel, A., Roset, X., Del Rio, J., Toma, D. M., Carreras, N., Panahi, S. S., et al. (2012). Ocean bottom seismometer: Design and test of a measurement system for marine seismology. *Sensors*, 12(3), 3693–3719. <https://doi.org/10.3390/s120303693>
- Marra, G., Clivati, C., Lockett, R., Tampellini, A., Kronjäger, J., Wright, L., et al. (2018). Ultrastable laser interferometry for earthquake detection with terrestrial and submarine cables. *Science*, 361(6401), 486–490. <https://doi.org/10.1126/science.aat4458>
- Marra, G., Fairweather, D. M., Kamalov, V., Gaynor, P., Cantono, M., Mulholland, S., et al. (2022). Optical interferometry-based array of seafloor environmental sensors using a transoceanic submarine cable. *Science*, 376(6595), 874–879. <https://doi.org/10.1126/science.abo1939>
- Martens, H. R., Rivera, L., & Simons, M. (2019). LoadDef: A Python-based toolkit to model elastic deformation caused by surface mass loading on spherically symmetric bodies. *Earth and Space Science*, 6(2), 311–323. <https://doi.org/10.1029/2018ea000462>
- Martens, H. R., Simons, M., Owen, S., & Rivera, L. (2016). Observations of ocean tidal load response in South America from subdaily GPS positions. *Geophysical Journal International*, 205(3), 1637–1664. <https://doi.org/10.1093/gji/ggw087>
- Meinig, C., Stalin, S. E., Nakamura, A. I., & Milburn, H. B. (2005). Real-time deep-ocean tsunami measuring, monitoring, and reporting system: The NOAA DART II description and disclosure. *NOAA, Pacific Marine Environmental Laboratory (PMEL)*, 1–15.
- Moeller, L. (2023). How the Moon impacts subsea communication cables. *arXiv preprint arXiv:2304.06905*.
- Pelaez Quiñones, J. D., Sladen, A., Ponte, A., Lior, I., Ampuero, J. P., Rivet, D., et al. (2023). High resolution seafloor thermometry for internal wave and upwelling monitoring using Distributed Acoustic Sensing. *Scientific Reports*, 13(1), 17459. <https://doi.org/10.1038/s41598-023-44635-0>
- Ray, R. D. (2013). Precise comparisons of bottom-pressure and altimetric ocean tides. *Journal of Geophysical Research: Oceans*, 118(9), 4570–4584. <https://doi.org/10.1002/jgrc.20336>
- Sladen, A., Rivet, D., Ampuero, J. P., De Barros, L., Hello, Y., Calbris, G., & Lamare, P. (2019). Distributed sensing of earthquakes and ocean-solid Earth interactions on seafloor telecom cables. *Nature Communications*, 10(1), 5777. <https://doi.org/10.1038/s41467-019-13793-z>
- Strobach, E., Klein, P., Molod, A., Fahad, A. A., Trayanov, A., Menemenlis, D., & Torres, H. (2022). Local air-sea interactions at ocean mesoscale and submesoscale in a western boundary current. *Geophysical Research Letters*, 49(7), e2021GL097003. <https://doi.org/10.1029/2021gl097003>
- Sutterley, T., Alley, K., Bishop-Taylor, R., Brunt, K., Howard, S., Padman, L., & Siegfried, M. (2025). pyTMD (Version 2.2.4) [Computer Software]. <https://doi.org/10.5281/zenodo.5555395>
- Tatekura, K., Yamamoto, H., & Ejiri, Y. (1982). Strain of optical fibres of an optical submarine cable on the sea bed. *Electronics Letters*, 18(10), 414–415. <https://doi.org/10.1049/el:19820284>
- Tonegawa, T., & Araki, E. (2024). High-frequency tsunamis excited near Torishima Island, Japan, observed by distributed acoustic sensing. *Geophysical Research Letters*, 51(11), e2024GL108714. <https://doi.org/10.1029/2024gl108714>
- Torres, H. S., Klein, P., Wang, J., Wineteer, A., Qiu, B., Thompson, A. F., et al. (2022). Wind work at the air-sea interface: A modeling study in anticipation of future space missions. *Geoscientific Model Development*, 15(21), 8041–8058. <https://doi.org/10.5194/gmd-15-8041-2022>
- Williams, E. F., Fernández-Ruiz, M. R., Magalhaes, R., Vanhillo, R., Zhan, Z., González-Herráez, M., & Martins, H. F. (2019). Distributed sensing of microseisms and teleseisms with submarine dark fibers. *Nature Communications*, 10(1), 5778. <https://doi.org/10.1038/s41467-019-13262-7>
- Williams, E. F., Ugalde, A., Martins, H. F., Becerril, C. E., Callies, J., Claret, M., et al. (2023). Fiber-optic observations of internal waves and tides. *Journal of Geophysical Research: Oceans*, 128(9), e2023JC019980. <https://doi.org/10.1029/2023jc019980>
- Young, W. C., Budynas, R. G., & Sadegh, A. M. (2002). *Roark's formulas for stress and strain* (Vol. 7, pp. 125–127). McGraw-Hill.
- Zhan, Z., Cantono, M., Kamalov, V., Mecozzi, A., Müller, R., Yin, S., & Castellanos, J. C. (2021). Optical polarization-based seismic and water wave sensing on transoceanic cables. *Science*, 371(6532), 931–936. <https://doi.org/10.1126/science.abe6648>
- Zumberge, M. A., Hatfield, W., & Wyatt, F. K. (2018). Measuring seafloor strain with an optical fiber interferometer. *Earth and Space Science*, 5(8), 371–379. <https://doi.org/10.1029/2018ea000418>